Astronomy & Astrophysics manuscript no. aa_paper_compile
August 13, 2026

Galactic panspermia by interstellar objects

Source populations, biosignature survival, and planetary delivery

Shokhruz Kakharov and Abraham Loeb

Astronomy Department, Harvard University, 60 Garden St., Cambridge, MA 02138, USA,
e-mail: shokhruzbekkakharov@college.harvard.edu; aloeb@cfa.harvard.edu

ABSTRACT

Context. Interstellar objects transport solid material between planetary systems and may also carry biological material or molecular biosignatures. Quantifying this transport requires connecting the Galactic populations that produce interstellar objects to their survival during interstellar travel and their eventual delivery to planets.

Aims. We investigate which stellar ages and Galactic components contribute to the interstellar-object population near the Sun, whether the locally detectable population is representative of the Galactic reservoir, and which processes limit the transfer of biosignature-bearing material between planetary systems.

Methods. We construct Monte Carlo populations that trace stellar formation in the thin disk, thick disk, bulge, halo, and satellites. Disk ages are drawn from the Milky Way star formation history reconstructed by Fantin et al. (2019), and age-dependent scale heights are used to calculate the population present near the Galactic midplane. We propagate these populations through local-flux, Vera C. Rubin Observatory detectability, and mission-accessibility selections. We then model three ejection histories and the survival of viable cells, amino-acid biosignatures, and refractory organics. Finally, we separate stellar-system encounter, perihelion activation, planet occurrence, debris interception, and biological survival in a Galactic delivery calculation. A separate Solar diagnostic calculates passages within 1 AU using the local velocity distribution and Solar gravitational focusing. The mass normalization is compared with the number density of objects the size of interstellar comet 3I/ATLAS, the third confirmed interstellar object.

Results. The local-flux population is moderately younger than the Galactic reservoir, with mean ages of 6.6 and 7.4 Gyr, respectively, and its icy fraction increases from 0.57 to 0.62. In the fiducial sample, 0.40 of the local objects satisfy the Rubin Observatory selection and 0.33 satisfy the adopted mission-accessibility cut. For the nominal local, late-uniform, impact-spallation branch, resistant frozen cells retain a probability of 0.044 after 100 Myr and 1.1×10^{-7} at 1 Gyr. No sampled impact carrier maintains a steady active brine, and the mean transient repair interval is only about 290 yr. Source access, loading, launch, and viable deposition suppress the resistant-cell result to 9.6×10^{-17} per ISO before target-system and planet interception, conditional on an inhabited source. The present-day focused rates within 1 AU of the Sun are 6.45 yr^{-1} for the adopted 1I/'Oumuamua-scale density and 0.452 yr^{-1} for the adopted 3I/ATLAS-scale density. These are optimistic heating and release opportunities, not planet deliveries. The observationally inferred 3I/ATLAS-sized density requires 7.6×10^{14} such objects per star, or about $9.1 \times 10^{3}\,M_\oplus$ of escaped material per star for a standard steep size distribution. For icy 3I/ATLAS that exceeds the ice/volatile stellar ceiling by a factor of 5.1 and the fiducial 1000 $M_\oplus$ yield by a factor of 9.1; a 0.42 km nucleus instead gives $9.4 \times 10^{2}\,M_\oplus$ and can fit both.

Conclusions. Local ISOs are not an unbiased Galactic sample. Physical viable-cell survival can remain non-negligible near 100 Myr but not generally at 1 Gyr, and loading plus planetary interception dominate the product. The nominal 3I/ATLAS mass package is inconsistent with the ice/volatile ceiling, while compact-nucleus and lower-density cases restore consistency. Absolute biological rates remain conditional on the unknown inhabited fraction and do not measure the origin or establishment of life.

Key words. astrobiology – panspermia – minor planets, asteroids: general – comets: general – Galaxy: stellar content

1. Introduction

Solid material is exchanged between planetary systems when planetesimals are ejected by planets, stellar companions, or the loss of mass from an evolving star. If an ejected body contains microorganisms or recognizable biological molecules, the same process provides a possible route for lithopanspermia between otherwise disconnected planetary systems (Melosh 2003; Wallis & Wickramasinghe 2004; Belbruno et al. 2012). This possibility involves more than survival in interstellar space. A carrier must first be produced and biologically loaded, escape its source system, remain intact during travel, enter another stellar system, and finally intersect a planet or release debris that does so.

The discoveries of 1I/2017 U1 ('Oumuamua), 2I/Borisov, and 3I/ATLAS establish that macroscopic bodies from other planetary systems pass through the Solar System (Meech et al. 2017; Guzik et al. 2020; Seligman et al. 2025). These objects also show that the observed interstellar-object (ISO) population is heterogeneous. 'Oumuamua appeared inactive at discovery, whereas Borisov and ATLAS displayed cometary activity. Their Galactic trajectories are consistent with different source ages: the current kinematic estimates place 'Oumuamua in a relatively young population, Borisov at an intermediate age, and ATLAS in an older population (Kakharov & Loeb 2026). Three objects, however, cannot determine the age, composition, or Galactic origin distribution of the underlying ISO reservoir.

The distinction between the Galactic reservoir and the population measured near the Sun is important for panspermia. The thin disk, thick disk, bulge, halo, and satellite populations have different star formation histories, metallicities, spatial distributions, and kinematics. Stellar scale height also increases with age, reducing the midplane density of old populations relative to their total Galactic abundance. A Solar-neighborhood sample can therefore overrepresent some source populations and underrepresent others. Detection introduces a second selection through object size, speed, brightness, activity, and survey geometry. The properties of the first detected ISOs should therefore not be assigned directly to the full Galactic population.

Previous panspermia calculations have examined individual parts of the transfer problem, including ejection, radiation survival, gravitational capture, and impact. Here we join these processes in one population model. We first construct an age- and component-resolved Galactic ISO reservoir. We then determine how Galactic structure and observational selection transform that reservoir into the local-flux, Rubin Observatory-detectable, and mission-accessible populations. Independently of this observational branch, we propagate biologically loaded carriers through interstellar travel, target-system encounter, perihelion activation, planet occurrence, and debris interception.

The absolute ISO supply is a major uncertainty. We retain a fiducial escaped mass yield of $1000\,M_\oplus$ per star and compare it with a separate 3I/ATLAS-based observational normalization (Hui et al. 2026), including the 0.42 km nongravitational-acceleration case of Thoss et al. (2026) and one-detection Poisson, activity, density, and size-slope sensitivities. The fiducial forward model is not forced to reproduce one observational inversion.

The purpose of this work is to identify which Galactic populations can supply potential panspermia carriers and which physical step most strongly limits their delivery. We now resolve biological loading into route-specific source access, incorporation, launch, and escape factors, and replace an imposed viable-cell lifetime with a dose- and population-based calculation. We do not calculate the probability that life originates in a source system. That unknown occurrence factor, and the probability that viable deposition leads to establishment, remain explicit sensitivities.

2. Galactic panspermia framework

2.1. Source-to-planet transfer

We divide the Galactic source population into bins s defined by Galactic component, stellar age, metallicity, formation radius, and rocky or icy composition. For a source bin s, the rate at which biologically loaded material reaches planets of class p can be written as

$$\dot{N}_{\mathrm{del},s,p} = \dot{N}_{\mathrm{ISO},s}\, f_{\mathrm{load},s}\, P_{\mathrm{surv},s}\, P_{\mathrm{sys},s}\, P_{\mathrm{act},s}\, f_p\, P_{\mathrm{hit},s,p}. \tag{1}$$

Here $\dot{N}_{\mathrm{ISO},s}$ is the ISO ejection rate from the source bin, $f_{\mathrm{load},s}$ is the fraction carrying the biological material under consideration, and $P_{\mathrm{surv},s}$ is its survival probability over the sampled travel time. The remaining terms are the probability of encountering a target stellar system, $P_{\mathrm{sys},s}$; the probability that the adopted perihelion condition activates or disrupts the carrier, $P_{\mathrm{act},s}$; the occurrence factor f_p for planet class p; and the conditional probability $P_{\mathrm{hit},s,p}$ that the activated material intersects that planet.

Summing over source bins and planet classes gives

$$\dot{N}_{\mathrm{del}} = \sum_s \sum_p \dot{N}_{\mathrm{del},s,p}. \tag{2}$$

We resolve $f_{\mathrm{load},s}$ into route-specific source access, incorporation, launch, and system-escape sensitivities. The fraction of source systems that are inhabited remains unknown, so the primary physical output is conditional on an inhabited source. Equation (1) retains the factors needed to apply any specified life-occurrence model.

2.2. Galactic supply and age dependence

The production term $\dot{N}_{\mathrm{ISO},s}$ is obtained from the stellar formation rate, the number of stars formed in each age bin, and the escaped ISO yield per star. We use the Milky Way star formation history reconstructed by Fantin et al. (2019). For disk populations, the contribution of an age bin to the density near the Sun is weighted by its vertical distribution. With an exponential vertical profile, the density of a cohort of age τ at height z is proportional to

$$w_z(\tau, z) = \frac{\exp[-|z|/h_z(\tau)]}{2h_z(\tau)}, \tag{3}$$

where $h_z(\tau)$ is the age-dependent scale height. This weighting is essential near the Galactic midplane: an old cohort can contain substantial total stellar mass while contributing a smaller local density because it is distributed through a larger vertical volume (Girardi et al. 2005).

The source calculation is performed separately for the thin disk, thick disk, bulge, halo, and satellites. Metallicity and formation radius affect the relative rocky and icy yields, while component kinematics affect transport and encounter speeds. The result is an age- and region-resolved supply of rocky and icy carriers rather than a single Solar-neighborhood population.

2.3. Survival and delivery probabilities

Survival and delivery are evaluated as distinct filters. For each carrier, we sample an ejection history and obtain a travel time bounded by the age of its source population. We consider viable cells, amino-acid biosignatures, and refractory organics. Viable cells use cumulative external and internal dose, organism state, initial abundance, loading, launch, thermal state, water activity, and repair conditions. The molecular carriers retain separate effective-lifetime sensitivities. None of these terms describes the emergence of life.

For surviving carriers, the target-system calculation is separated into system encounter, activation, planet occurrence, and debris interception. Keeping these steps separate shows where the suppression comes from when the final probability is small. We evaluate log-uniform, geometric, and gravitational-focusing perihelion models and report each factor in Eq. (1) in the results.

2.4. Observational branch and fair-sample test

The observational calculation branches from the Galactic reservoir rather than from the delivery chain. It maps the reservoir into four samples: the local ISO flux, objects detectable by Rubin Observatory, objects detected with early warning, and objects satisfying an adopted mission-accessibility cut. Comparisons between these stages quantify selection in age, metallicity, formation radius, speed, Galactic component, size, and rocky or icy composition.

This branch addresses how observations should be interpreted. It does not imply that an object must pass through the Solar neighborhood or be detectable by Rubin Observatory before contributing to panspermia elsewhere in the Galaxy. Its role is to determine whether the population available to observers is a reliable tracer of the source terms entering Eq. (1).

The complete framework therefore has two connected outputs. The first is an observationally selected population used to test whether local ISOs represent the Galactic reservoir. The second is a source-to-planet probability budget used to determine which source populations and physical bottlenecks control conditional Galactic panspermia.

3. Galactic source population and ISO normalization

3.1. Stellar components

We represent the Milky Way with a stellar disk, bulge, stellar halo, and a population of surviving and disrupted satellites. The analytic density model uses a disk mass of $5 \times 10^{10}\,M_\odot$, radial scale length $R_\mathrm{d} = 2.6$ kpc, and vertical scale $z_\mathrm{d} = 0.3$ kpc. The bulge has a stellar mass of $10^{10}\,M_\odot$ and a Hernquist scale radius of 0.6 kpc. The total stellar-halo mass is $1.4 \times 10^{9}\,M_\odot$ and is divided into in-situ and accreted contributions. Fifty satellites are generated from analytic mass and spatial distributions; tidally disrupted systems contribute to the accreted halo. These components provide the spatial densities and velocity mixture used to construct the local ISO flux. The adopted scales are intended as a smooth population model rather than a reconstruction of individual streams or merger remnants (Bland-Hawthorn & Gerhard 2016; Helmi 2020).

For the demographic fair-sample calculation, we use five source labels: thin disk, thick disk, bulge, halo, and satellites. The reference Galactic reservoir is assigned broad mass-like fractions of 0.55, 0.22, 0.16, 0.04, and 0.03, respectively. These fractions define a comparison reservoir; they are not fitted to the three detected ISOs. The dynamical model contains a single disk component, so local disk objects are divided statistically into thin- and thick-disk labels. Their mean fractions are calibrated to the local stellar mass densities inferred by Fantin et al. (2019), $0.036\,M_\odot\,\mathrm{pc}^{-3}$ for the thin disk and $0.0045\,M_\odot\,\mathrm{pc}^{-3}$ for the thick disk. Earth-relative speed retains kinematic information within this split: high-speed disk objects have a larger relative thick-disk probability, while the mean split remains fixed by the local density ratio.

3.2. Age distribution and vertical weighting

Disk ages are drawn from a digitization of the total Milky Way star formation history in Fig. 9 of Fantin et al. (2019). Monte Carlo ages are sampled by inverse transform of the trapezoidally integrated native digitization. For population figures and mass accounting, we separately evaluate a cubic interpolant on a 1 Myr grid over 0–13.5 Gyr, truncate negative interpolation artifacts, and integrate the result into 1 Gyr bins, with a final 13–13.5 Gyr bin. The Fantin curve is not component resolved. We therefore do not assign different star formation histories to the thin and thick disks; the labels carry spatial, chemical, and kinematic information, while both disk labels draw ages from the published total history.

The non-disk components use truncated Gaussian age distributions. The bulge, halo, and satellite means are 10, 12, and 9 Gyr, with standard deviations 1.8, 0.9, and 2.4 Gyr, respectively. All sampled ages are restricted to 0.02–13.5 Gyr. These distributions are phenomenological population priors and are varied only through the component mixture in the present calculation.

To convert the global formation history into the age distribution near the midplane, we use the age-dependent exponential scale height

$$h_z(\tau) = 95\,\mathrm{pc}\left(1 + \frac{\tau}{4.4\,\mathrm{Gyr}}\right)^{1.66}, \tag{4}$$

following Girardi et al. (2005). The unnormalized local contribution of age bin i is

$$W_i = \int_{\tau_i}^{\tau_{i+1}} \mathrm{SFR}(\tau)\frac{\exp[-|z_\odot|/h_z(\tau)]}{2h_z(\tau)}\,\mathrm{d}\tau. \tag{5}$$

We adopt $R_\odot = 8.34$ kpc and $z_\odot = 17$ pc for this calculation. The weights $W_i/\sum_j W_j$ are calibrated to a total local disk mass density of $0.0405\,M_\odot\,\mathrm{pc}^{-3}$. With an assumed mean stellar mass of $0.5\,M_\odot$, the corresponding local number density is 0.081 stars pc^{-3}. This age-cohort calculation uses the Fantin radial scale length of 2.3 kpc. It is kept distinct from the 2.6 kpc scale used by the forward dynamical disk.

3.3. Metallicity, formation radius, and carrier composition

Each source label is assigned distributions in formation radius and metallicity. The thin disk is centered at $R_\mathrm{birth} = 8.0$ kpc with a 2.4 kpc dispersion, while the thick disk is centered at 7.0 kpc with a 2.3 kpc dispersion. The corresponding mean metallicities are −0.04 and −0.55 dex. The bulge, halo, and satellites have mean metallicities of −0.10, −1.55, and −1.05 dex. Their adopted formation radii are centered at 2, 12, and 35 kpc, respectively. These broad priors represent population-level source environments, not recovered birth locations of individual ISOs.

For the thin disk, we apply

$$[\mathrm{Fe/H}] = [\mathrm{Fe/H}]_0 + \gamma\,(R_\mathrm{birth} - 8\,\mathrm{kpc}) + \epsilon_\mathrm{Fe}, \tag{6}$$

where ϵ_Fe is the component metallicity scatter. We calculate separate realizations for $\gamma = -0.03$, -0.05, and -0.07 dex kpc^{-1}, spanning the range of disk-gradient sensitivities used here (Willett et al. 2023).

The probability that a carrier is icy is parameterized as

$$P_\mathrm{icy} = \mathrm{clip}\left[P_\mathrm{icy,0} - 0.08[\mathrm{Fe/H}] + 0.015\left(\frac{\tau}{\mathrm{Gyr}} - 5\right), 0.05, 0.95\right]. \tag{7}$$

The baseline values $P_\mathrm{icy,0}$ are 0.60, 0.46, 0.30, 0.35, and 0.50 for the thin disk, thick disk, bulge, halo, and satellites. This relation is a simple composition model used to test selection and survival; it is not an empirical measurement of ISO composition as a function of age. The rocky probability is $P_\mathrm{rocky} = 1 - P_\mathrm{icy}$.

3.4. Size distribution and fixed-yield model

Object radii are sampled from

$$\frac{\mathrm{d}N}{\mathrm{d}R} = AR^{-q}, \qquad R_\mathrm{min} \le R \le R_\mathrm{max}. \tag{8}$$

Our fiducial convention uses $q = 3$, $R_\mathrm{min} = 50$ m, and $R_\mathrm{max} = 10$ km. We also evaluate $q = 2.5$ as a shallower sensitivity case. This is a differential radius distribution; the sign and differential versus cumulative convention must therefore be specified when comparing with other ISO size-frequency distributions (Marčeta & Seligman 2023). The forward population uses a bulk density of $2\,\mathrm{g\,cm^{-3}}$ and geometric albedo $p = 0.1$. Its normalization is rescaled to a fixed escaped ISO mass

$$M_{\mathrm{ISO},\star} = 1000\,M_\oplus \tag{9}$$

per star. This value is a fiducial yield, not a ceiling and not a fit to an observed local density.

3.5. Normalization to 3I/ATLAS

As an independent observational diagnostic, we use the current estimate $n_\mathrm{3I} = 7.0 \times 10^{-3}\,\mathrm{AU}^{-3}$ for 3I/ATLAS-sized objects and an effective radius $R_\mathrm{3I} = 1.3 \pm 0.2$ km (Hui et al. 2026).

The published density is an order-of-magnitude estimate rather than a reported confidence interval. We attach external one-count Garwood intervals of 1.2×10^{-3}–$2.3 \times 10^{-2}\,\mathrm{AU}^{-3}$ at 68% and 1.8×10^{-4}–$3.9 \times 10^{-2}\,\mathrm{AU}^{-3}$ at 95% (Garwood 1936). These intervals represent counting uncertainty only; survey selection, cometary activity, and size systematics remain outside them.

Under a constant escaped yield per star, the required number of 3I/ATLAS-sized objects is

$$\eta_{3I} = \frac{n_{3I}(206265)^3}{n_{\star,\odot}}, \tag{10}$$

where 206265 is the number of AU per parsec and $n_{\star,\odot} = 0.081\,\mathrm{pc}^{-3}$. This gives $\eta_{3I} = 7.6 \times 10^{14}$ objects per star. To convert number into mass we adopt a comet-like density of $0.5\,\mathrm{g\,cm^{-3}}$; this density is an assumption and is not measured by Hui et al. (2026). Extending the normalization over Eq. (8) gives $9.1 \times 10^3\,M_\oplus$ per star for $q = 3$. The result is 9.1 times the fixed yield in Eq. (9). We therefore report a fixed-yield forward model and a separate 3I-normalized mass requirement. The observational inversion does not overwrite the forward normalization.

The photometric radius and survey density are not independent direct measurements of a bare nucleus because 3I/ATLAS was active. As a separate sensitivity, Thoss et al. (2026) infer a 0.42 km radius when the measured nongravitational acceleration is dominated by CO_2 sublimation and 0.74–1.15 km when water contributes more strongly. We therefore compute a joint grid over radius cases from 0.42 to 2.8 km, bulk densities of 0.3, 0.5, and $1.0\,\mathrm{g\,cm^{-3}}$, and differential slopes $q = 2.5$, 3.0, and 3.5. For each grid point we propagate the exact central one-detection Garwood interval for the survey density.

We also define an explicit activity-selection factor

$$f_{\mathrm{act}} = \frac{n_{\mathrm{physical}}}{n_{\mathrm{survey}}}, \tag{11}$$

where $f_{\mathrm{act}} < 1$ represents an active coma causing a survey-derived normalization larger than the physical density of comparable nuclei. We show $f_{\mathrm{act}} = 0.1$, 0.3, 1, and 3 only as sensitivity axes; they are not assigned confidence levels because the present survey sample does not measure this correction. This prevents an assumed activity correction from being mistaken for a resolution of the discrepancy.

For a single body, mass scales as ρR^3. That scaling cannot be applied directly to the full size-distribution result. When a measured density is interpreted as $N(R \geq R_{3I})$, changing R_{3I} also changes the normalization of $\mathrm{d}N/\mathrm{d}R$. We therefore recompute the power-law integrals at every radius instead of multiplying the $9.1 \times 10^3\,M_\oplus$ result by R^3.

The required escaped mass must also fit within the material available to a source star. Because 3I/ATLAS is treated as an icy/volatile-dominated body, the composition-relevant absolute-material ceiling is the stellar oxygen-and-carbon inventory converted into ice,

$$M_{\mathrm{ice,max}} = M_{\mathrm{H_2O}} + M_{\mathrm{CO_2}}, \tag{12}$$

where all carbon is placed in CO_2 (consuming the stoichiometric oxygen) and leftover oxygen is placed in H_2O. We adopt generous upper mass fractions $f_{\mathrm{O}} = 0.008$ and $f_{\mathrm{C}} = 0.0025$. Equation (12) gives $1.78 \times 10^3\,M_\oplus$ for the adopted $0.5\,M_\odot$ mean star and $3.55 \times 10^3\,M_\oplus$ for a $1\,M_\odot$ star. For absolute contrast we also retain a deliberately generous all-metal ceiling,

$$M_{Z,\mathrm{max}} = Z_{\mathrm{max}} M_\star, \qquad Z_{\mathrm{max}} = 0.02, \tag{13}$$

and a rock-forming metal ceiling $M_{\mathrm{rock,max}} = f_{\mathrm{rock}} M_\star$ with $f_{\mathrm{rock}} = 0.002$ (Si+Mg+Fe scale), equal to $3.33 \times 10^3\,M_\oplus$ and $3.33 \times 10^2\,M_\oplus$ for the adopted mean star. The rock ceiling is contrast only: it is not the 3I/ATLAS budget test. All three ceilings assume 100% conversion and ejection. Comparisons with the required escaped mass are reported in Sect. 7.1.

4. Monte Carlo transport and observational selection

4.1. Local dynamical sample

We draw 10^4 velocity realizations from the local mixture of Galactic components. For each component, stellar velocities are represented by a three-dimensional Gaussian with a component-dependent bulk motion and velocity ellipsoid. An isotropic Maxwellian ejection kick is then added to the stellar velocity. Component weights are set by their local ISO density, and the random component counts are drawn from the corresponding multinomial distribution. The same realization provides object sizes, component labels, Galactocentric velocities, and detection distances used in the fair-sample analysis.

For observational and mission calculations, velocities are transformed to a fixed Earth-relative convention. We adopt the Solar peculiar velocity $(U, V, W) = (11.1, 12.24, 7.25)\,\mathrm{km\,s^{-1}}$ relative to the local standard of rest from Schönrich et al. (2010) and add an assumed circular speed of $220\,\mathrm{km\,s^{-1}}$ to the azimuthal component. The resulting Solar Galactocentric velocity is $(11.1, 232.24, 7.25)\,\mathrm{km\,s^{-1}}$. We also subtract a $29.78\,\mathrm{km\,s^{-1}}$ terrestrial orbital contribution in the adopted azimuthal direction. This approximation provides a consistent speed for all selection stages; it does not average over the Earth's orbital phase.

The demographic attributes are attached statistically after the dynamical sample is constructed. In particular, disk ages are not inferred separately from each sampled velocity. The speed affects the relative thin/thick label, but both disk labels draw age from the total Fantin star formation history. This prevents the model from manufacturing separate component age curves not provided by the digitized data, while retaining a kinematic ranking within the local disk.

4.2. Detection-distance model

For radius R and geometric albedo p, we use the asteroid magnitude conversion

$$H = 5\log_{10}\left[\frac{1329\ \mathrm{km}}{(2R/1000)\sqrt{p}}\right], \tag{14}$$

where R is in meters. Assuming heliocentric and geocentric distances are approximately equal, the apparent magnitude is $m = H + 10\log_{10}(d/\mathrm{AU})$. The limiting magnitude $m_{\mathrm{lim}} = 24.5$ then gives

$$d_{\mathrm{max}} = 10^{(m_{\mathrm{lim}}-H)/5}\ \mathrm{AU}. \tag{15}$$

This is a simple brightness proxy. It omits a full cadence, phase-function, activity, weather, and trailing-loss simulation. The resulting Rubin Observatory categories should therefore be interpreted as comparative selection functions rather than a survey forecast (Ivezić et al. 2019; Marčeta & Seligman 2023).

4.3. Population stages

The fair-sample calculation compares independently sampled Galactic-reservoir and local-flux distributions. It does not follow the same labeled object from its birth location to the Sun. The reservoir provides the denominator for demographic bias, while the local distribution reuses the dynamical ISO sample. Within each metallicity-gradient realization, all objects have weight $1/N$ before selection.

We define the following stages:

1. *Galactic reservoir*: the five-component reference mixture described in Sect. 3.
2. *Local flux*: all 10^4 objects in the local velocity and size realization.
3. *Rubin Observatory detectable*: objects with $d_{\max} \geq 3$ AU.
4. *Rubin Observatory early warning*: objects with $d_{\max} \geq 10$ AU.
5. *Mission accessible*: Rubin Observatory-detectable objects satisfying the adopted impulsive deflection requirement.

For the mission proxy, the warning time is

$$t_{\rm lead} = \frac{d_{\max}}{v_{{\rm rel},\oplus}}, \tag{16}$$

and the velocity change required to remove a miss distance b is

$$\Delta v_{\rm req} = \frac{b}{t_{\rm lead}}. \tag{17}$$

We use $b = 0.1$ AU and define the primary accessible sample by $\Delta v_{\rm req} \leq 2.02\ {\rm km\,s^{-1}}$. Additional cuts at 4, 7, and 12 ${\rm km\,s^{-1}}$ are retained as sensitivity cases. This metric tests warning-time and velocity-change selection only; it is not a complete spacecraft trajectory or launch-window calculation (Hoover et al. 2022).

4.4. Bias estimators and reproducibility

For every population stage and metallicity gradient, we record weighted rocky and icy yields, mean age, mean metallicity, median speed, formation radius, and component fractions. If X_k is a weighted quantity in stage k, its reservoir-relative bias is

$$B_X(k) = \frac{X_k}{X_{\rm reservoir}}. \tag{18}$$

The flux-weight bias measures the retained fraction of the reference sample, whereas the rocky and icy biases show how selection changes the potential carrier budget.

The primary sample contains 10^4 Monte Carlo objects for each of the three metallicity gradients. We retain the full object-level sample, rather than summary moments alone, so that changes in age, metallicity, source component, speed, size, and composition can be recomputed at every selection stage. Monte Carlo fractions are reported together with their underlying counts where they enter rare-event interpretations.

5. Biosignature survival during interstellar travel

5.1. Travel-time scenarios

The age of a source star is not the travel time of an ISO. We therefore draw the time since ejection separately, while requiring it not to exceed the stellar age. For a source age $t_\star$, the early-ejection model is

$$t_{\rm tr} = t_\star U(0.70, 1.00), \tag{19}$$

where $U(a, b)$ denotes a uniform random variable. This case represents planetesimals expelled during or soon after planetary-system formation, so their interstellar residence time is most of the source age.

The late-uniform model assumes no preferred ejection epoch,

$$t_{\rm tr} = U(0, t_\star). \tag{20}$$

It includes both recent and ancient ejections and can represent continued scattering or ejection during late stellar evolution.

The recent-ejection model is an exponential sensitivity case,

$$t_{\rm tr} = \min\left[t_\star, X_{\exp}(1\ {\rm Gyr})\left(\frac{60\ {\rm km\,s^{-1}}}{v}\right)\right], \tag{21}$$

where $X_{\exp}$ is exponentially distributed and v is the available relative speed. The speed factor lengthens the time for slow objects under a fixed characteristic path scale. At $v = 60\ {\rm km\,s^{-1}}$, the probability of drawing $t_{\rm tr} < 10$ Myr before the stellar-age truncation is $1 - \exp(-10/1000) \simeq 0.01$. Thus, very short flights do not dominate this scenario.

Travel times are stored in 10 Myr bins centered at 5, 15, 25 Myr, and so on. Using bin centers prevents a formally zero path length in the subsequent target-system calculation. This imposes a 5 Myr numerical floor, including for the rare sampled source younger than 5 Myr. These three histories are limiting prescriptions, not ejection-time distributions inferred from observations. The survival calculation uses this 10 Myr resolution, while the survival-versus-time figure averages it into 1 Gyr bins to suppress finite-sample changes in the rocky and icy mixture.

5.2. Rocky and icy shielding geometries

For each object we draw a rocky or icy channel using the probabilities in Eq. (7). Biological material is then assigned to a surface, buried, or deep-interior layer. For icy objects the probabilities are 0.25, 0.45, and 0.30, respectively. For rocky objects they are 0.45, 0.40, and 0.15. Surface depths are sampled between 10^{-3} and 0.05 m, buried depths between 0.05 and 2 m, and deep-interior depths between 2 and 20 m. Every depth is capped at $0.8R$, where R is the object radius, so the shielding geometry remains possible for small bodies.

This depth model follows the strong dependence of radiation exposure on depth found in lithopanspermia and planetary-radiation studies (Mileikowsky et al. 2000; Horneck et al. 2001; Dartnell et al. 2007). It does not explicitly transport individual cosmic-ray species, secondary particles, or radionuclide products through each sampled composition.

5.3. Biological loading and launch

Generic ISO production is not biological loading. We resolve the loading factor in Eq. (1) into

$$P_{\rm load|inh} = P_{\rm source}\,P_{\rm incorporate}\,P_{\rm esc}, \tag{22}$$

conditional on an inhabited source. Launch survival is retained separately. We evaluate impact-spalled rock, later incorporation of planetary ejecta into a comet, cryovolcanic plume material, moon or ring ejecta, atmospheric grazing, tidal disruption, post-main-sequence release, and exo-Oort leakage. Impact spallation is the principal experimentally anchored route: selected organisms can survive part of the low-shock ejecta tail, but survival depends strongly on pressure, host-rock porosity, and organism

(Horneck et al. 2008). The other routes are sensitivity branches. Plume particles, for example, must first aggregate or become buried in a larger body before they provide meaningful interstellar shielding (Klenner et al. 2024). Comet incorporation is a two-stage hypothesis (Wallis & Wickramasinghe 2004); atmospheric grazing, tidal disruption, post-main-sequence release, and exo-Oort erosion are constrained by dynamical calculations but not by measured biological loading fractions (Siraj & Loeb 2020; Raymond et al. 2018; Veras et al. 2014; Hanse et al. 2018).

For each route we draw source access, incorporation, launch survival, system escape, atmospheric entry, and deposition from explicit log-uniform ranges. These ranges are hypotheses, not confidence intervals. We retain $f_{\rm inhabited} = (10^{-6}, 10^{-3}, 0.1, 1)$ and $P_{\rm establish} = (10^{-12}, 10^{-6}, 10^{-3}, 1)$ as external sensitivities. Cluster transfer is not counted as a loading mechanism because it changes transport after loading (Belbruno et al. 2012). Likewise, post-main-sequence and exo-Oort release can only export biological material that entered the body earlier.

5.4. Dose-based viable-cell model

For viable cells we replace the imposed gigayear lifetime with cumulative dose and population survival. The overburden column is

$$\Sigma = \rho d, \tag{23}$$

and the external dose rate is interpolated from a transport envelope $\dot{D}_{\rm GCR}(\Sigma)$. The envelope includes shallow secondary-particle buildup: its nominal values are 0.10 Gy yr^{-1} at zero column, 0.15 Gy yr^{-1} at 100 kg m^{-2}, 3×10^{-3} Gy yr^{-1} at 2000 kg m^{-2}, and 10^{-4} Gy yr^{-1} at 10^4 kg m^{-2}. A factor-of-two normalization range represents differences among radiation-transport calculations (Mileikowsky et al. 2000; Dartnell et al. 2007). This tabulated envelope is a population-level surrogate, not object-specific particle transport.

Shielding cannot remove radiation produced inside the carrier. We draw internal dose rates of 10^{-4}–2×10^{-4} Gy yr^{-1} for rocky material and 10^{-6}–3×10^{-5} Gy yr^{-1} for icy mixtures. We represent 70% of this term by ^{40}K with half-life 1.248 Gyr and 30% by longer-lived radionuclides. The integrated dose is

$$D(t) = \dot{D}_{\rm GCR} t + \dot{D}_{\rm int} 10^6 \left[0.7 \frac{1 - \exp(-\lambda_K t)}{\lambda_K} + 0.3 t \right], \tag{24}$$

where t is in Myr and $\lambda_K = \ln 2/1248$ Myr^{-1}. The internal term is motivated by the radiation limit calculated for spores in salt inclusions (Kminek et al. 2003).

We use three biological states. The conservative-spore branch draws $D_{10} = 1.5$–2.5 kGy. The resistant frozen-cell branch draws $D_{10} = 10$–50 kGy to bracket an optimistic extrapolation from frozen and desiccated polyploid cells. Laboratory endpoints reach 140 kGy for frozen, desiccated *D. radiodurans*, whereas tested bacterial spores are sterilized near 12 kGy (Horne et al. 2022); these acute endpoints do not measure a gigayear survival law. We also draw chemical-damage half-lives of 0.2–10 Myr and 1–100 Myr, respectively. These broad ranges expose the unmeasured decay of repair proteins and other macromolecules rather than claiming a calibrated low-temperature rate.

For an initial population N_0, launch probability $P_{\rm launch}$, and single-cell logarithmic survival

$$\log_{10} S_{\rm cell} = -\frac{D_{\rm eq}}{D_{10}} - \frac{t_{\rm dormant}}{t_{1/2,\rm chem}} \log_{10} 2, \tag{25}$$

the expected viable population and probability of retaining at least one cell are

$$N_{\rm viable} = N_0 P_{\rm launch} S_{\rm cell}, \tag{26}$$

$$P_{\geq 1} = 1 - \exp(-N_{\rm viable}). \tag{27}$$

The second equation supplies the Poisson probability relevant to a rare remaining cell; it prevents a fractional population from being described as a successful carrier.

5.5. Speculative active-brine upper bound

The third biological state permits repair only when a protected niche passes four tests simultaneously: local temperature at least 253 K, water activity at least 0.635, radiolytic chemical power of at least 1 zW per initial cell, and both electron-donor and electron-acceptor availability. The local temperature follows steady spherical conduction,

$$T(r) = T_s + \frac{\rho q_{\rm rad}}{6k}(R^2 - r^2), \tag{28}$$

and the conductive cooling time is R^2/κ. If steady heating does not maintain the temperature threshold, repair lasts for at most this cooling time. During an allowed active interval we remove 99% of dose-equivalent damage; the remainder of the flight follows the frozen-cell model. The active and resistant-frozen branches use the same D_{10} and chemical-damage draws, so their difference isolates the effect of permitted repair.

This branch is deliberately an upper bound. Ordinary 0.1–10 km bodies cool far faster than a gigayear, and radiogenic heating that supplies chemical energy also supplies an internal radiation dose. A cold brine with low water activity or no usable redox pair is therefore not counted as an active ecosystem. The maintenance-power scale is informed by terrestrial ice and sediment communities (Price & Sowers 2004; Morono et al. 2020), but no observation establishes a gigayear liquid ecosystem in an ISO.

5.6. Legacy molecular-carrier sensitivity

For comparison with the earlier calculation, amino-acid biosignatures and refractory organics retain the effective-lifetime prescription

$$P_{\rm surv} = \exp\left(-\frac{t_{\rm tr}}{\tau_{\rm eff}}\right). \tag{29}$$

The previous 1 Gyr viable-cell prescription is retained only as a legacy comparison case. It is not the fiducial viable-life result. Keeping them separate prevents molecular persistence or an imposed lifetime from being presented as evidence for living cells.

Terrestrial preservation provides context, not an interstellar calibration. Viable bacteria have been cultured from Siberian permafrost assigned an age near 3.5 Myr (Zhang et al. 2013). Communities from 101.5 Myr marine sediment resumed metabolism during incubation (Morono et al. 2020), which supports long-lived energy-limited communities rather than one identified cell remaining dormant for 101.5 Myr. The reported bacterium from 250 Myr New Mexico salt remains disputed (Vreeland et al. 2000; Hazen & Roedder 2001; Kminek et al. 2003). None of these observations demonstrates one-gigayear dormant survival under interstellar irradiation.

5.7. Monte Carlo construction and summaries

The calculation is applied to every metallicity-gradient and population-stage group. The legacy molecular comparison uses at most 2.5×10^4 Monte Carlo objects per group, whereas the physical calculation uses 250 weighted source draws per group and evaluates three biological states, eight loading routes, and three ejection histories for each draw. Reservoir radii are resampled from the local size distribution and missing speeds are assigned $60\ \mathrm{km\,s^{-1}}$.

The physical calculation follows all steps: source access, incorporation, launch survival, system escape, overburden column, external and internal dose, thermal state, water activity, maintenance power, initial and expected viable-cell numbers, atmospheric entry, deposition, and $P_{\geq 1}$. Results are reported at the sampled travel time and at fixed times of 1, 10, 100, and 1000 Myr. Weighted means include 68% and 95% Monte Carlo sampling intervals. If no sampled object survives, we report the approximate 95% upper limit $3/N_{\mathrm{eff}}$ rather than calling the probability zero. Life occurrence and establishment are treated only as separate sensitivity factors because they are not measured by this calculation.

6. Target-system encounters and planetary delivery

6.1. Statistical target population

Delivery targets are drawn from a smooth axisymmetric density model rather than a catalog of known exoplanets. The target stellar density in $\mathrm{pc^{-3}}$ is

$$n_\star(R,z) = 0.09 \exp\left[-\frac{R-8\,\mathrm{kpc}}{2.6\,\mathrm{kpc}}\right] \exp\left(-\frac{|z|}{0.3\,\mathrm{kpc}}\right) + 0.5 \exp\left(-\frac{R}{0.7\,\mathrm{kpc}}\right) \exp\left(-\frac{|z|}{0.5\,\mathrm{kpc}}\right) + 10^{-4}\left[\frac{\max(\sqrt{R^2+z^2}, 1\,\mathrm{kpc})}{8\,\mathrm{kpc}}\right]^{-3}. \quad (30)$$

The three terms are disk, bulge, and halo proxies. We sample $0.2 < R < 18$ kpc and $-3 < z < 3$ kpc with probability proportional to $R\,n_\star(R,z)$, including the cylindrical annular-volume factor.

The target metallicity is

$$[\mathrm{Fe/H}]_{\mathrm{target}} = \mathrm{clip}\left[-0.04 + \gamma(R - 8\,\mathrm{kpc}) - 0.12|z|, -1.8, 0.6\right], \quad (31)$$

where R and z are in kpc and each object retains the metallicity-gradient case of its parent sample. Equations (30) and (31) define a statistical target field, not a claim that every point in the Galaxy has a known planetary system.

6.2. Stellar-system encounter probability

For an object traveling for t_{tr} at speed v, the straight-line path length is

$$L_{\mathrm{pc}} = 1.022712 \left(\frac{v}{\mathrm{km\,s^{-1}}}\right)\left(\frac{t_{\mathrm{tr}}}{\mathrm{Myr}}\right). \quad (32)$$

We define a target-system encounter as passage within $b_{\mathrm{sys}} = 100$ AU. For local target density $n_\star$, the expected number of encounters is

$$\mu_{\mathrm{sys}} = n_\star \pi \left(\frac{b_{\mathrm{sys}}}{206265}\right)^2 L_{\mathrm{pc}}, \quad (33)$$

and the Poisson probability of at least one encounter is

$$P_{\mathrm{sys}} = 1 - \exp(-\mu_{\mathrm{sys}}). \quad (34)$$

This calculation approximates the path as sampling the density assigned to the target draw. It does not integrate a time-dependent Galactic orbit through spiral structure or correlated stellar environments.

6.3. Perihelion and activation models

An encounter within 100 AU does not guarantee that an icy carrier is heated, disrupted, or otherwise activated. We therefore compare three distributions for the perihelion distance q_{tar} between 0.05 and 100 AU.

The *log-uniform* case draws $\ln q_{\mathrm{tar}}$ uniformly and is an optimistic sensitivity model because it assigns substantial probability to small perihelia. The *geometric* case draws an area-weighted impact parameter

$$b = 100\sqrt{U(0,1)}\ \mathrm{AU} \quad (35)$$

and sets $q_{\mathrm{tar}} = b$. The *gravitational-focusing* case uses the same impact parameter and maps it to a Solar-mass perihelion,

$$q_{\mathrm{tar}} = \frac{1}{2}\left[-\alpha + \sqrt{\alpha^2 + 4b^2}\right], \qquad \alpha = \left(\frac{42.1\ \mathrm{km\,s^{-1}}}{v}\right)^2 \mathrm{AU}. \quad (36)$$

In all cases, activation is represented by the indicator

$$P_{\mathrm{act}} = \mathbf{1}(q_{\mathrm{tar}} \leq 3\ \mathrm{AU}). \quad (37)$$

The threshold is an activation proxy. It does not assert that every carrier inside 3 AU disrupts or that every carrier outside 3 AU remains inactive.

6.4. Solar habitable-zone passage diagnostic

The target-system calculation above asks whether one traveling ISO encounters another star. We separately ask the inverse observational question: how often the present local ISO population passes within 1 AU of the Sun. This does not require a prior 100 AU encounter draw. For local ISO number density n_{ISO} and heliocentric speed distribution $p(v_\infty)$, the focused passage rate is

$$\Gamma(< q_{\mathrm{HZ}}) = n_{\mathrm{ISO}} \int p(v_\infty)\, \pi q_{\mathrm{HZ}}^2 \left[1 + \frac{v_{\mathrm{esc}}^2(q_{\mathrm{HZ}})}{v_\infty^2}\right] v_\infty\, \mathrm{d}v_\infty, \quad (38)$$

where $q_{\mathrm{HZ}} = 1$ AU and $v_{\mathrm{esc}}(1\ \mathrm{AU}) = 42.1\ \mathrm{km\,s^{-1}}$. The geometric comparison omits the term in square brackets. We evaluate the integral with the nominal local-flux Earth-relative velocity sample rather than a single characteristic speed (Eubanks et al. 2021).

We report the 1I-scale normalization $n_{1\mathrm{I}} = 0.1\ \mathrm{AU^{-3}}$ and the 3I/ATLAS-like normalization $n_{3\mathrm{I}} = 7.0 \times 10^{-3}\ \mathrm{AU^{-3}}$ separately. The latter is a 3I-like survey normalization and is not treated as a measured cumulative density above a sharp radius. Both densities originate from one-object inferences, so we attach central Garwood intervals for one count (Garwood 1936). For a stationary duration $T = 5$ Gyr, the expected passage count is

$$\lambda_{\mathrm{HZ}} = \Gamma(< 1\ \mathrm{AU})T. \quad (39)$$

At fixed λ_{HZ} the realized count is Poisson distributed. Extrapolating the present density and velocity distribution for 5 Gyr is a sensitivity calculation, not a reconstruction of the Solar System's time-dependent Galactic environment.

For the survival-weighted diagnostic, a passage within 1 AU is assumed optimistically to heat the carrier and permit release of biologically loaded material. We use representative radii of 50 m for the 1I-scale class and 1.3 km for the 3I/ATLAS-scale class, draw shielding with the same prescription as in the survival calculation, and compare legacy effective-lifetime scales of 0.1 and 1 Gyr. These panels are retained as molecular-carrier sensitivities; they are not the dose-based viable-cell result in Sect. 5.4. The resulting count is conditional on biological loading. Passage within 1 AU does not guarantee debris interception by a habitable planet, viable deposition, or colonization.

6.5. Planet occurrence and orbital sampling

We consider rocky habitable-zone planets, sub-Neptunes, and cold giants. Their base occurrence factors are 0.25, 0.35, and 0.10. We apply the metallicity scaling

$$f_p([\mathrm{Fe/H}]) = \mathrm{clip}\left[f_{p,0}10^{\beta_p[\mathrm{Fe/H}]}, 0, 0.95\right], \tag{40}$$

with $\beta_p = 0.25$, 0.55, and 1.6, respectively. The weak scaling for rocky planets and stronger scaling for giant planets follow the qualitative host-metallicity trends in exoplanet surveys (Fischer & Valenti 2005; Wang & Fischer 2015; Petigura et al. 2018).

Semimajor axes are sampled uniformly in $\ln a$ over 0.5–1.7 AU for rocky habitable-zone planets, 0.05–1 AU for sub-Neptunes, and 2–10 AU for cold giants. Planet radii are fixed at 1, 2.5, and 11.2 Earth radii. These distributions are population-level sensitivity prescriptions and do not include multiplicity, eccentricity, mutual inclination, or correlations between planet classes.

6.6. Debris interception

Activated fragments are assigned an isotropic ejecta speed $v_{\mathrm{ej}} = 0.5\ \mathrm{km\,s^{-1}}$. The characteristic angular spread is

$$\theta_{\mathrm{ej}} = \mathrm{clip}\left(\frac{v_{\mathrm{ej}}}{v}, 10^{-8}, 0.2\right), \tag{41}$$

and the radial width at perihelion is

$$\Delta r = \max(0.01 q_{\mathrm{tar}}, \theta_{\mathrm{ej}} q_{\mathrm{tar}}). \tag{42}$$

For a planet at semimajor axis a, the orbit-overlap factor is

$$P_{\mathrm{overlap}} = \exp\left[-\frac{1}{2}\left(\frac{a - q_{\mathrm{tar}}}{\Delta r}\right)^2\right]. \tag{43}$$

The conditional geometric interception probability is then

$$P_{\mathrm{hit}} = P_{\mathrm{overlap}} \frac{R_p}{\pi a}, \tag{44}$$

bounded to the interval $[0, 1]$. The planet-occurrence-weighted probability used below is $f_p P_{\mathrm{hit}}$.

This is a toy debris-interception model, not an N-body treatment of fragment trajectories, comet tails, radiation pressure, or capture. A separate straight-line diagnostic samples release radii, encounter speeds, and ejecta speeds. If that diagnostic produces no realized impacts, we report the finite-sample limit $1/N$ rather than interpreting the result as a physically exact zero.

6.7. Combined delivery probability and Monte Carlo sampling

For each carrier and planet class, the raw and survival-weighted delivery probabilities are

$$P_{\mathrm{del,raw}} = P_{\mathrm{sys}} P_{\mathrm{act}} f_p P_{\mathrm{hit}}, \tag{45}$$

$$P_{\mathrm{del,surv}} = P_{\mathrm{del,raw}} P_{\mathrm{surv}}. \tag{46}$$

For viable cells we also report

$$P_{\mathrm{del,viable|inh}} = P_{\mathrm{del,raw}} P_{\mathrm{load|inh}} P_{\geq 1} P_{\mathrm{entry}} P_{\mathrm{deposition}}, \tag{47}$$

$$P'_{\mathrm{establish}} = f_{\mathrm{inhabited}} P_{\mathrm{del,viable|inh}} P_{\mathrm{establish}}. \tag{48}$$

The first remains conditional on an inhabited source. The second is shown only across the explicit occurrence and establishment sensitivities; neither factor is inferred from the ISO sample.

The delivery calculation retains the Galactic-reservoir, local-flux, and mission-accessible stages. If their combined size exceeds 6×10^4 Monte Carlo objects, we reduce the sample and rescale weights to preserve the original total. The same target positions and planet orbits are used for all three activation models so that differences arise from perihelion sampling rather than different target realizations.

Results are grouped by source component, metallicity gradient, population stage, activation model, ejection history, carrier class, loading route, and planet class. We report the mean system-encounter, activation, occurrence-weighted hit, survival, raw-delivery, and survival-weighted delivery probabilities separately. A reported zero can therefore mean that no qualifying event occurred at the finite Monte Carlo resolution; it is not interpreted as proof of a zero physical probability.

7. Results

7.1. Age-resolved ISO supply and the 3I/ATLAS mass budget

The digitized Fantin star-formation history places its largest formed-mass fractions in the 9–10 and 10–11 Gyr bins, which contain 0.17 and 0.16 of the integrated history. The age-dependent scale height changes this ordering near the Galactic plane. The scale height rises from 114 pc at 0.5 Gyr to 641 pc at 9.5 Gyr and 720 pc at 10.5 Gyr. After vertical weighting and normalization at the Solar position, the corresponding local age fractions are 0.17, 0.09, and 0.08. Thus, the old peak in the integrated formation history remains present, but the youngest 1 Gyr bin makes the largest individual contribution to the local midplane population.

Matching $n_{3\mathrm{I}} = 7.0 \times 10^{-3}\ \mathrm{AU^{-3}}$ at the calibrated local density 0.0810 stars $\mathrm{pc^{-3}}$ requires 7.6×10^{14} 3I/ATLAS-sized bodies per star (Sect. 3.5). At 0.5 $\mathrm{g\,cm^{-3}}$, those bodies alone contain 584 $M_\oplus$ per star; the full $q = 3$ distribution raises the escaped mass to 9.1×10^3 $M_\oplus$ per star, of which 87% lies above the 1.3 km threshold. That requirement is 9.1 times the fiducial 1000 $M_\oplus$ yield, 5.1 times the ice/volatile ceiling, 2.7 times the $Z = 0.02$ all-metal ceiling, and 27 times the rock-forming contrast ceiling. Equivalently, the fixed-yield model would need a local stellar density of 0.737 $\mathrm{pc^{-3}}$. With the recent-SFR anchor, the inferred $q = 3$ population requires 6.37×10^4 $M_\oplus\,\mathrm{yr^{-1}}$ of escaped material, whereas the fixed yield supplies 7.00×10^3 $M_\oplus\,\mathrm{yr^{-1}}$. For $q = 2.5$ the requirement rises to 1.31×10^4 $M_\oplus$ per star; the independent forward-model inversion gives 1.76×10^4 $M_\oplus$ per star as a cross-check with different Galactic assumptions.

Compatibility with the ice ceiling at fixed remaining parameters requires a 3I-like density $\lesssim 1.4 \times 10^{-3}\ \mathrm{AU^{-3}}$, a radius $\lesssim 0.578$

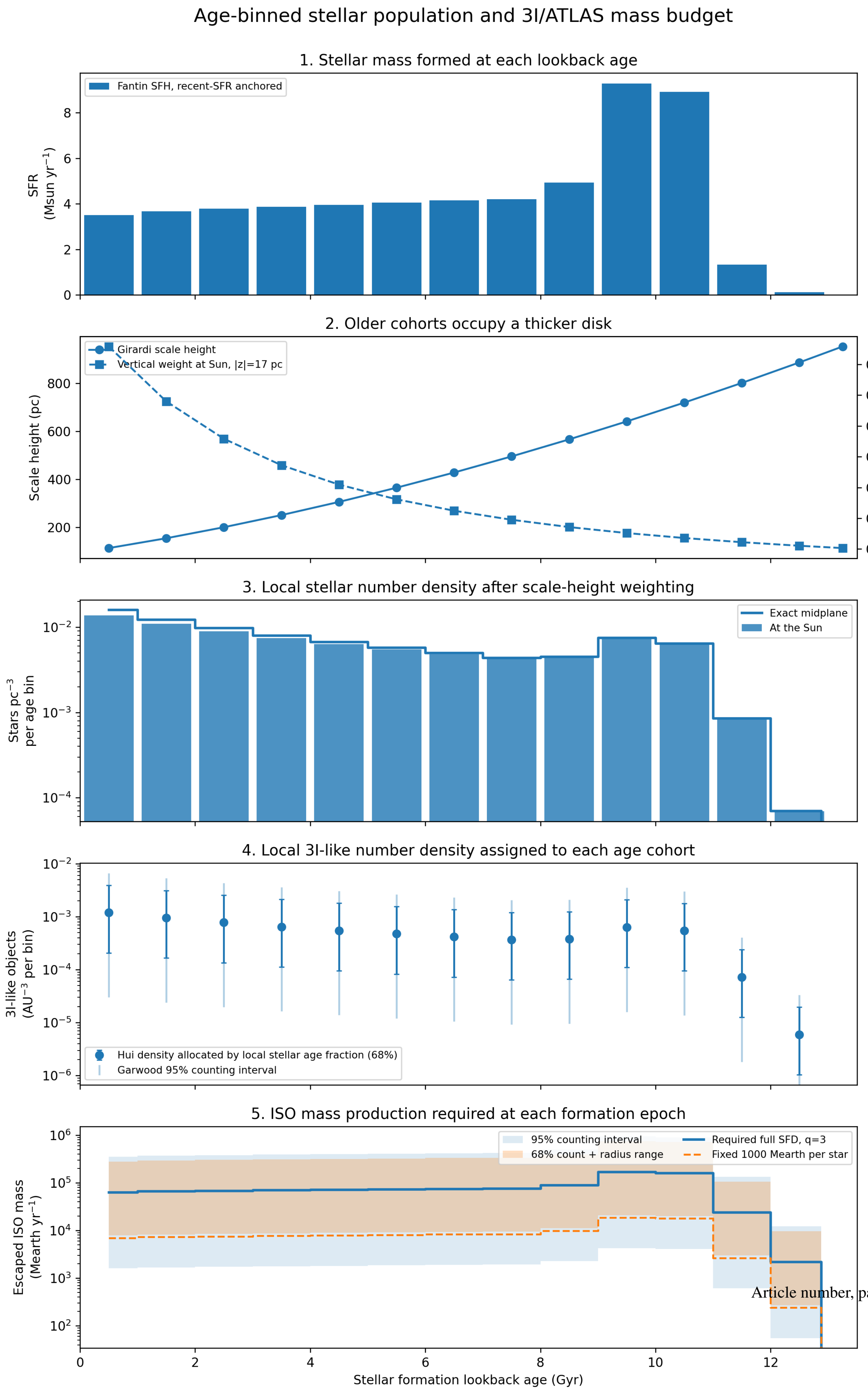
Age-binned stellar population and 3I/ATLAS mass budget
1. Stellar mass formed at each lookback age
Fantin SFH, recent-SFR anchored
SFR (Msun yr⁻¹)
2. Older cohorts occupy a thicker disk
Girardi scale height
Vertical weight at Sun, |z|=17 pc
Scale height (pc)
Vertical weight (pc⁻¹)
3. Local stellar number density after scale-height weighting
Exact midplane
At the Sun
Stars pc⁻³ per age bin
4. Local 3I-like number density assigned to each age cohort
Hui density allocated by local stellar age fraction (68%)
Garwood 95% counting interval
3I-like objects (AU⁻³ per bin)
5. ISO mass production required at each formation epoch
95% counting interval
68% count + radius range
Required full SFD, q=3
Fixed 1000 Mearth per star
Escaped ISO mass (Mearth yr⁻¹)
Stellar formation lookback age (Gyr)

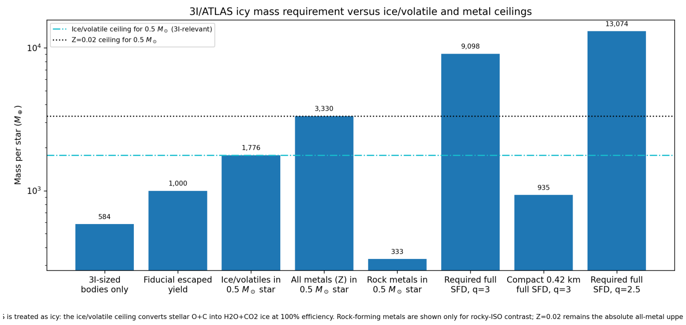

Fig. 2: Mass-per-star comparison for icy 3I/ATLAS between the 3I-sized population, the fiducial escaped yield, the ice/volatile O+C ceiling, the $Z = 0.02$ all-metal ceiling, the rock-forming metal ceiling (rocky-ISO contrast only), and the full size-distribution requirements. Ceilings assume 100% conversion and ejection and therefore overestimate the physically available escaped ISO mass.

km, or $f_{\rm act} \lesssim 0.195$ at 1.3 km; the fixed yield needs $\lesssim 0.434$ km or $f_{\rm act} \lesssim 0.110$. The compact 0.42 km case gives 935 $M_\oplus$ per star (one-count 68% range 163–3076 $M_\oplus$), which fits both the fixed yield and the ice ceiling at the nominal density. At 1.3 km the $q = 3$ one-count mass interval is 1.59×10^3–2.99×10^4 $M_\oplus$ at 68%. These are counting intervals and scenario axes, not a joint posterior (Hui et al. 2026; Seligman et al. 2025; Loeb 2025). A pure R^3 rescaling is inappropriate for the full-SFD mass because changing the threshold also changes the normalization of dN/dR.

The inferred ages of the three known ISOs occupy different parts of this distribution. Their median ages and 68% intervals are 3.2 [0.5, 8.8] Gyr for 1I, 5.0 [1.8, 9.7] Gyr for 2I, and 8.7 [5.2, 10.3] Gyr for 3I. The broad intervals overlap, and these three posteriors do not determine the population weights used above.

7.2. Bias between the Galactic reservoir and local samples

We use $\gamma = -0.05$ dex kpc^{-1} as the nominal metallicity-gradient case. The reservoir and local-flux catalogs each contain 10000 Monte Carlo objects. Of the local objects, 3984 pass the Rubin Observatory selection and 3264 pass the primary mission-accessibility cut.

The reservoir has mean age 7.43 Gyr, median age 8.43 Gyr, and a weighted 16–84% interval of 3.08–10.59 Gyr. The local flux is younger, with mean 6.63 Gyr, median 7.26 Gyr, and interval 2.41–10.15 Gyr. The Rubin Observatory and mission-accessible means are 6.64 and 6.62 Gyr, respectively. Therefore the largest age change occurs between the reservoir and the Solar-neighborhood flux. Rubin Observatory detection and the adopted accessibility cut add little further age bias.

The mean metallicity changes from −0.25 in the reservoir to −0.10 in the local flux, −0.10 in the Rubin Observatory sample, and −0.09 in the accessible sample. The mean formation radius changes more weakly, from 7.79 to 7.90, 7.92, and 7.91 kpc. The shift toward higher metallicity is therefore not caused by a large change in mean formation radius alone. It also reflects the removal of most halo and satellite sources from the local sample.

The reservoir component fractions are 0.55 thin disk, 0.22 thick disk, 0.16 bulge, 0.04 halo, and 0.03 satellites. In the local flux these become 0.88, 0.11, less than 0.01, less than 0.01, and effectively zero, respectively. The mission-accessible sample is 0.90 thin disk, 0.10 thick disk, and less than 0.01 bulge, with no halo or satellite object in this finite sample. This component replacement explains both the younger local mean and its higher mean metallicity.

The mean Earth-relative speed is 62.01 km s^{-1} in the local flux, 62.15 km s^{-1} after the Rubin Observatory selection, and 55.10 km s^{-1} after the accessibility cut. The corresponding medians are 59.58, 59.52, and 54.10 km s^{-1}. Accessibility is therefore the only stage among these two observational selections that produces a clear numerical speed shift.

The expected icy fraction rises from 0.57 in the reservoir to 0.62 in the local flux, Rubin Observatory sample, and accessible sample. The local icy-to-reservoir bias factor is 1.09, while the rocky factor is 0.89. Across $\gamma = -0.03$, -0.05, and -0.07 dex kpc^{-1}, the local mean ages span only 6.63–6.65 Gyr and the local icy fraction remains approximately 0.62. The metallicity-gradient sensitivity is therefore smaller than the reservoir-to-local component change for these observables. We describe these as numerical differences; the present output does not contain a formal hypothesis test for their statistical significance.

The component bars alone do not predict a discovery ratio between 1I/'Oumuamua-like and 3I/ATLAS-like objects. With the adopted $q = 3$ size distribution there are simply more small bodies than large ones: integrating from a representative 1I radius of 75 m and from the adopted 3I radius of 1.3 km gives approximately 300 bodies above the 1I scale for every body above the 3I scale. Across the 50–100 m radius range used as an illustrative 1I scale, the ratio is approximately 170–680. Observed discoveries need not follow that number ratio because small inactive objects have much smaller survey volumes, whereas active comets can be detected at larger distances. A quantitative observed ratio therefore requires a common size-, activity-, and survey-selection calculation.

Conditioning the nominal local-flux catalog on the published 3I/ATLAS 68% age interval of 5.2–10.3 Gyr selects 5190 of 10000 objects. Its median [Fe/H] is −0.07, with a 16–84% interval of −0.35 to 0.16. We convert this model metallicity prior into a deliberately generous proxy $Z_{\rm upper} = \min[0.02, 0.02\, 10^{\rm [Fe/H]}]$. For the adopted $0.5\, M_\odot$ star, the resulting median complete heavy-element inventory is 2.84×10^3 $M_\oplus$, with a 16–84% interval of 1.49–3.33×10^3 $M_\oplus$. The required 9.1×10^3 $M_\oplus$ of escaped ISO mass is therefore 3.2 times the median complete metal inventory.

The 10–12 Gyr sensitivity selects 1850 objects and has median [Fe/H] = −0.08. Its median heavy-element ceiling is 2.77×10^3 $M_\oplus$, making the required escaped mass 3.3 times the median ceiling. No selected Monte Carlo row in either age window contains enough total heavy-element mass to meet the nominal $q = 3$ requirement, even before accounting for planet formation or ejection efficiency. This is a projection of the adopted fair-sample demographic prior, not an independently measured age-metallicity relation.

7.3. Physical microbial viability and biological loading

The dose calculation changes the interpretation of long travel. Increasing burial first removes ultraviolet and low-energy particle exposure, but the external GCR dose approaches a penetrating-particle floor and the internal radionuclide dose continues to accumulate. Therefore, shielding does not create an unlimited lifetime. The relevant result is the probability that at least one member of an initially finite population remains viable.

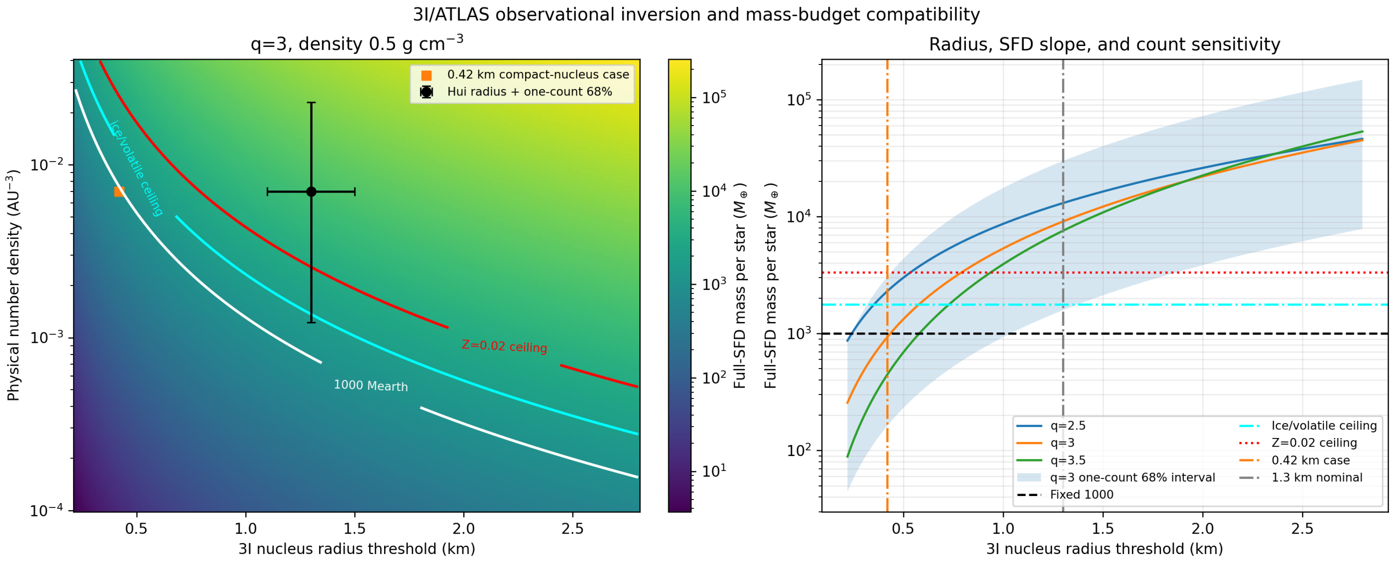

Fig. 3: Joint observational sensitivity of the 3I/ATLAS mass inversion. The left panel shows the full $q = 3$ size-distribution mass as a function of the physical nucleus-radius threshold and number density for $\rho = 0.5\,\mathrm{g\,cm^{-3}}$. The black point and error bars show the 1.3 ± 0.2 km radius and exact one-detection 68% Garwood density interval; the orange square marks the 0.42 km nongravitational-acceleration case at the nominal density. White, cyan, and red contours denote the fixed $1000\,M_\oplus$ yield, the ice/volatile ceiling relevant to icy 3I/ATLAS, and the deliberately generous $Z = 0.02$ all-metal ceiling. The right panel shows radius and SFD-slope sensitivity at nominal density; the shaded region is the $q = 3$ one-count 68% interval. Radius, slope, bulk density, and activity corrections are scenario axes, not a joint measured confidence region.

For the nominal local-flux, late-uniform, impact-spallation branch, the mean sampled travel time is 3.30 Gyr. At fixed travel times of 1, 10, 100, and 1000 Myr, the conservative-spore probabilities are 0.12, 0.029, 4.2×10^{-14}, and 4.1×10^{-147}. The resistant frozen-cell probabilities are 0.18, 0.12, 0.044, and 1.1×10^{-7}. Thus, the physical model permits a several-percent resistant-cell population result at 100 Myr, but not a generally high gigayear survival fraction.

No impact-spallation draw in this group maintains a steady active habitat. The active-brine branch has a mean allowed active interval of only 2.9×10^{-4} Myr, or about 290 yr, and therefore gives the same fixed-time results as the resistant frozen-cell branch to the quoted precision. An internal liquid ecosystem therefore does not solve the gigayear problem for the sampled ordinary ISO sizes. It would require a different carrier class or heat source, not merely deeper burial.

At the sampled travel times, the mean probability of at least one viable cell is 7.3×10^{-7} for conservative spores and 0.0040 for resistant frozen cells. After source access, incorporation, launch, and system escape, these become 3.8×10^{-16} and 2.1×10^{-12} per ISO conditional on an inhabited source. Including entry and viable deposition gives 1.4×10^{-20} and 9.6×10^{-17}. Among 250 Monte Carlo draws there are zero conservative-spore survivors and one resistant-cell survivor; the corresponding zero-count 95% upper limit is 0.012 and is much weaker than the continuous expected probability.

The route comparison shows why generic ISO production cannot be converted directly into a panspermia rate. Impact spallation has the strongest experimental basis, while the icy routes require an additional incorporation or burial step. Post-main-sequence release and exo-Oort leakage efficiently remove existing bodies but do not explain how those bodies were loaded. The reported viable-deposition probability therefore retains every route factor and remains conditional on an inhabited source.

The legacy gigayear effective-lifetime curves are retained only for amino acids, refractory organics, and comparison with the previous calculation. They are not used to claim microbial survival. The physical viable-cell results instead identify the unusual combination of a large initial population, favorable launch, deep shielding, low internal radioactivity, and short travel required for a non-negligible result.

7.4. Solar passages through the nominal habitable-zone scale

The nominal local-flux sample contains 10000 velocity draws and has a weighted mean Earth-relative speed of $62.01\,\mathrm{km\,s^{-1}}$. For the $0.1\,\mathrm{AU^{-3}}$ 1I-scale normalization, the geometric passage rate within 1 AU is 4.11 $\mathrm{yr^{-1}}$ and Solar focusing raises it to 6.45 $\mathrm{yr^{-1}}$. The corresponding stationary 5 Gyr expectation is 3.23×10^{10} passages. Propagating the external one-count 68% Garwood density interval gives 5.63×10^{9}–1.06×10^{11} passages; the 95% interval is 8.17×10^{8}–1.80×10^{11}.

For the nominal $7.0 \times 10^{-3}\,\mathrm{AU^{-3}}$ 3I/ATLAS-like normalization, the geometric and focused rates are 0.288 and 0.452 $\mathrm{yr^{-1}}$. The 5 Gyr expectation is 2.26×10^{9}, with a one-count 68% density interval of 3.94×10^{8}–7.43×10^{9} and a 95% interval of 5.72×10^{7}–1.26×10^{10}. At fixed nominal density, ordinary Poisson counting fluctuations are only of order $\sqrt{\lambda}$ and are negligible relative to the one-detection density intervals. The uncertainty is therefore set by population normalization and survey systematics, not by counting billions of passages once the rate is fixed.

For late-uniform ejection, reducing the legacy base lifetime from 1 Gyr to 0.1 Gyr changes the conditional survival fractions from 0.49 to 0.11 for the legacy viable-cell curve, 0.55 to 0.14 for amino-acid biosignatures, and 0.61 to 0.16 for refractory organics. The 1I-scale survival-weighted 5 Gyr opportunities are therefore $(3.41, 4.45, 5.19) \times 10^{9}$ for the 0.1 Gyr cases and $(1.58, 1.77, 1.96) \times 10^{10}$ for the 1 Gyr cases. For

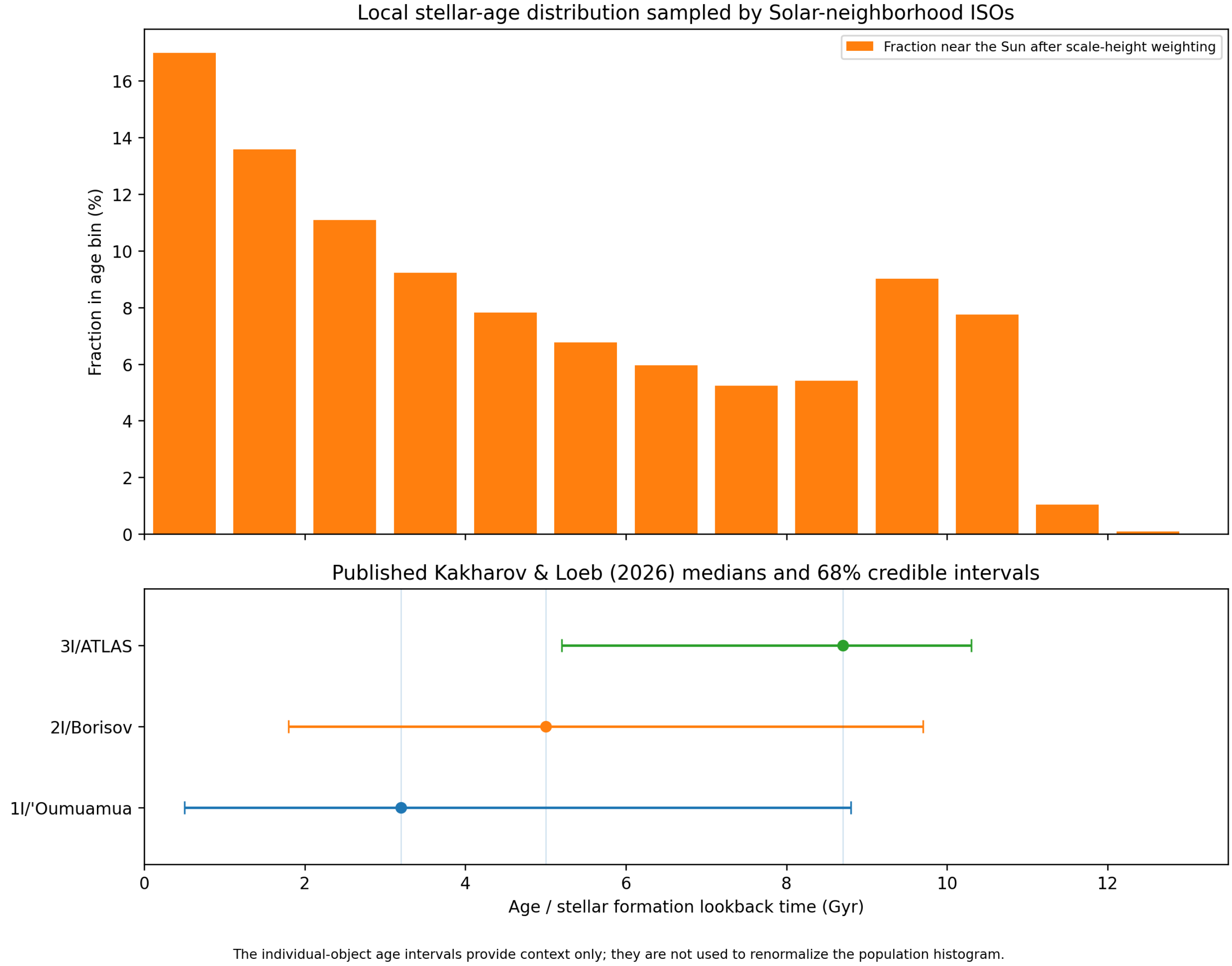

Fig. 4: Top: stellar-age fractions near the Sun after applying the age-dependent scale-height weighting to the digitized Fantin history. This local distribution, rather than the Galaxy-wide formation history, is the comparison population for detected ISOs. Bottom: published median ages and 68% intervals for 1I, 2I, and 3I. The individual-object posteriors are shown for context and are not used to normalize the population histogram.

the 3I/ATLAS-scale normalization, the corresponding ranges are $2.41–3.63 \times 10^8$ and $1.11–1.37 \times 10^9$. These values remain conditional release opportunities, not successful panspermia events.

7.5. The delivery bottleneck

The delivery calculation uses stratified sampling so each metallicity-gradient, population-stage, ejection-history, biological-state, and loading-route group retains up to 100 source objects. This gives 72 900 source objects before evaluating three activation prescriptions and three planet classes. Across this sample the mean activation fractions are 0.539 for log-uniform perihelia, 9×10^{-4} for geometric perihelia, and 1.2×10^{-3} with gravitational focusing.

For a concrete physical case, consider the nominal local, late-uniform, resistant frozen-cell, impact-spallation branch and rocky habitable-zone planets. Its mean system-encounter probability is 0.0359. In the log-uniform perihelion model, the activation fraction is 0.58 and the raw probability through system encounter, activation, planet occurrence, and debris interception is 1.25×10^{-9}. Multiplying by transit viability gives 1.15×10^{-15}. Carrying source access, incorporation, launch, system escape, entry, and deposition through the same rows reduces the probability to 2.28×10^{-29} per ISO conditional on an inhabited source. The fiducial $P_{\rm establish} = 10^{-6}$ sensitivity gives 2.28×10^{-35} before multiplying by $f_{\rm inhabited}$.

The geometric and focusing realizations contain no activated row in this 100-row physical subgroup, and therefore no resolved viable delivery. Their rule-of-three limit is 0.03 on the unresolved Monte Carlo row fraction. It is not a 0.03 upper limit on physical delivery, because the system encounter, planet occurrence, debris geometry, loading, survival, and deposition factors still multiply that fraction. These zero groups show that ordinary Monte Carlo sampling does not resolve the small-perihelion and planet-crossing phase space.

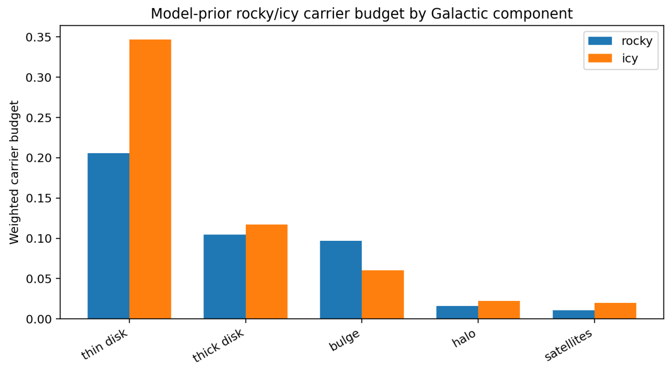

Fig. 5: Rocky and icy contributions separated by Galactic source component. The broad component context follows Galactic-structure reviews (Bland-Hawthorn & Gerhard 2016; Helmi 2020), but the plotted reservoir fractions $(0.55, 0.22, 0.16, 0.04, 0.03)$ for the thin disk, thick disk, bulge, halo, and satellites are explicit model priors rather than a fit to satellite data. The change in component mixture between the reservoir and local flux produces the composition bias discussed in Sect. 7.2.

7.6. Conditional source contributions and the missing absolute rate

The earlier component split obtained by summing equally weighted carrier classes is not an absolute biological source split. The physical calculation includes eight route hypotheses whose occurrence rates are unknown and must not be averaged as if each route were equally common. Component contributions are therefore reported separately for each loading route, biological state, and ejection history. The geometric and focusing perihelion models also remain too sparse for a stable component split.

The present results do not yet provide an absolute $\dot{N}_{\rm delivered}$ by both source region and stellar-age bin. The age-budget calculation supplies an age-resolved production rate, while the delivery calculation supplies conditional probabilities by component, but the two products are not joined object by object or bin by bin. Multiplying their separately averaged values would discard correlations among age, component, travel time, speed, survival, and target encounter probability. We therefore do not report an absolute Galactic panspermia rate. The directly supported result is the conditional probability chain and its source-component weighting.

8. Discussion

8.1. Young midplane populations and old interstellar objects

The Fantin history and Girardi scale height answer different questions. The formation history counts the stellar mass formed throughout the disk, where the 9–11 Gyr interval is prominent. The vertical correction asks which of those populations remain concentrated near the plane. Because h_z increases with age, the local density per unit formed mass decreases. The youngest bin is then the largest local bin, while the old formation peak remains in the integrated history.

The fair-sample calculation adds a second selection. Bulge, halo, satellite, and part of the thick-disk reservoir contribute little to the Solar neighborhood flux, reducing the mean age from 7.43 to 6.63 Gyr. A detected object with an old posterior, such as the 8.7 Gyr median inferred for 3I, is therefore compatible with the model, but old objects are not required to dominate the local flux. The current calculation neither proves a thick-disk origin for 3I nor uses its age posterior to force the Galactic age distribution.

8.2. Does icy material have a survival advantage?

Icy objects increase from 0.57 of the reservoir supply to about 0.62 of the local supply. In the physical model, icy mixtures also draw a lower internal radionuclide dose and can contain more pore ice. These advantages do not imply that icy bodies are loaded more often. Primordial comets have little direct contact with inhabited crust, while plume grains require aggregation and burial before ejection. Rocky impact spalls have a clearer loading route but higher internal dose and more severe launch shock.

The route-resolved calculation now includes incorporation and ejection sterilization, but it still does not model the origin of life. The unknown $f_{\rm inhabited}$ can reverse any rocky or icy ordering inferred from transport alone. The output therefore reports each route separately rather than averaging them into one empirical loading fraction.

8.3. Normalization tension

Section 7.1 shows that the nominal Hui density, 1.3 km radius, $q = 3$ distribution, and $0.5\,{\rm g\,cm^{-3}}$ density cannot all describe a physically available icy reservoir: the required escaped mass exceeds the ice/volatile ceiling and the fixed $1000\,M_\oplus$ yield. The compact-nucleus and lower-density cases remove that tension, so the inconsistency diagnoses the observational package rather than proving an impossible ejected ice mass. The quoted mass is escaped ISO mass; if only a fraction $f_{\rm esc}$ escapes, the required source reservoir scales as $1/f_{\rm esc}$. The age-conditioned metallicity prior in Sect. 7.2 tightens the metal comparison further, but it is a prior projection rather than an empirical age-metallicity relation. Activity-selection factors that restore consistency quantify the correction that would be needed; they do not measure it.

8.4. Viable life requires more than shielding

Section 7.3 reverses the imposed gigayear-lifetime conclusion: shielding does not remove the penetrating and internal dose floors, resistant cells can remain non-negligible near 100 Myr, and conservative spores have already collapsed by then. The active-brine branch does not rescue ordinary sampled carriers. Legacy molecular effective lifetimes must not be read as viable-cell survival. Loading, launch, deposition, and establishment can each dominate the product even when transit viability is nonzero.

The delivery calculation (Sect. 7.5) exposes a modeling uncertainty more than a measured rate. Optimistic log-uniform perihelia give delivery probabilities near 10^{-9}, while geometric and focusing perihelia remain unresolved. Reliable estimates need importance sampling of small perihelia and planet-crossing debris, not only larger ordinary Monte Carlo samples.

8.5. What the Solar-neighborhood sample can test

The local and Rubin Observatory-selected samples are similar in age, metallicity, formation radius, speed, and icy fraction. Rubin Observatory selection therefore does not strongly distort the already-local population under the present detection model. The main bias occurs earlier, between the Galactic reservoir and the local flux. Rubin Observatory can test the local distributions with

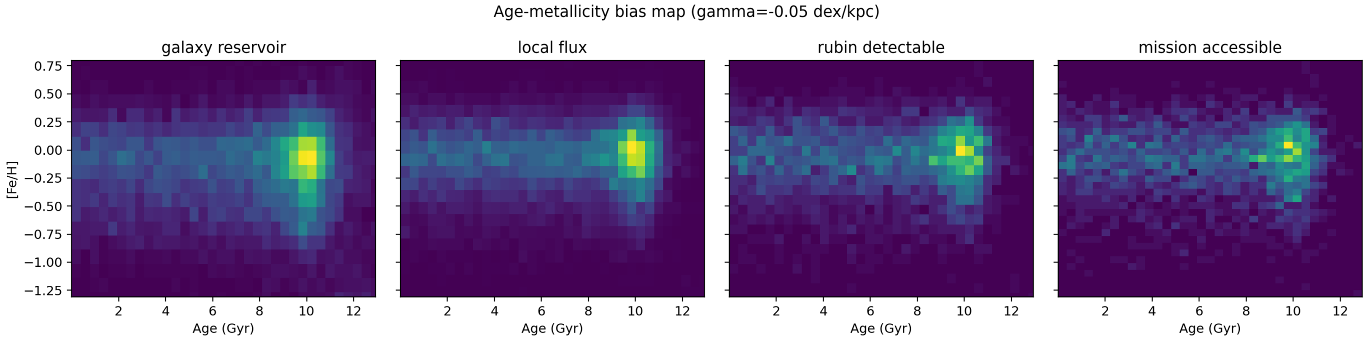

Fig. 6: Age-metallicity distributions at the reservoir, local-flux, Rubin Observatory-detectable, and mission-accessible stages for the plotted $\gamma = -0.05$ dex kpc^{-1} case. The dominant change occurs between the Galactic reservoir and the local flux.

a larger sample, but converting those measurements into Galactic reservoir fractions will still require a model of component-dependent transport and survey selection.

The three known ISOs span broad and overlapping age posteriors. They show that individual dynamical ages can be estimated, but they do not yet measure the age distribution, the rocky-to-icy ratio, or the frequency of old thick-disk objects. A larger sample could test whether the predicted local mean near 6.6 Gyr and icy fraction near 0.62 are consistent with the observed population. Such a comparison also requires consistent activity and size selection, particularly because an active 3I-like comet is not selected in the same way as an inactive 1I-like body.

8.6. Scope of the present panspermia constraint

The calculation supports three statements. Galactic structure makes the Solar-neighborhood ISO population an incomplete representation of the reservoir. Favorable resistant-cell populations can retain several-percent viability at 100 Myr, but ordinary shielding does not establish high gigayear viability. Biological loading, launch, and viable deposition add major suppressions before perihelion activation and planetary interception.

It does not yet support an absolute number of successful panspermia events. The fraction of inhabited source systems and establishment probability are unknown, the route priors are not measured occurrence rates, the physical debris-interception probability is unresolved, and the production and delivery products have not been combined by source age and component. The next calculation needed for the central rate is a joint, importance-sampled population that carries each age-resolved production weight through loading, survival, target encounter, activation, and planetary interception. Until that calculation is made, the results are a conditional probability budget rather than a measured Galactic panspermia rate.

9. Conclusions

Local ISOs are not an unbiased copy of the Galactic reservoir: they are younger, more metal-rich, thinner-disk dominated, and slightly icier, while Rubin Observatory selection adds little further demographic bias (Sect. 7.2). An old peak in the integrated star formation history also does not dominate the midplane once scale-height weighting is included (Sect. 7.1).

For icy 3I/ATLAS, the nominal survey density and 1.3 km nucleus imply about $9.1 \times 10^3\, M_\oplus$ of escaped material per star—about 5 times the ice/volatile stellar ceiling and 9 times the fiducial $1000\, M_\oplus$ yield. Compact-nucleus or lower physical-density cases restore consistency, so the tension diagnoses the observational package rather than a feasible ejected ice mass (Sect. 7.1).

Physical viable-cell survival can remain at the percent level near 100 Myr for resistant carriers, but not generally at 1 Gyr; loading and deposition suppress the resistant-cell probability to $\sim 10^{-16}$–10^{-17} per ISO before planetary interception, conditional on an inhabited source (Sect. 7.3). Habitable-zone passages are activation opportunities, not deliveries; optimistic log-uniform planetary delivery remains $\sim 10^{-29}$ per ISO after the full chain (Sects. 7.4 and 7.5). Absolute Galactic panspermia rates still require unknown inhabited fractions, establishment probabilities, and a joint age-resolved delivery calculation.

Acknowledgements. This work was supported in part by Harvard University, the Origins of Life Initiative, the Black Hole Initiative, and the Galileo Project.

References

Belbruno, E., Moro-Martín, A., Malhotra, R., & Savransky, D. 2012, Astrobiology, 12, 754
Bland-Hawthorn, J., & Gerhard, O. 2016, ARA&A, 54, 529
Dartnell, L. R., Desorgher, L., Ward, J. M., & Coates, A. J. 2007, Biogeosciences, 4, 545
Eubanks, T. M., Hein, A. M., Lingam, M., et al. 2021, arXiv e-prints, arXiv:2103.03289
Fantin, N. J., Côté, P., McConnachie, A. W., et al. 2019, ApJ, 887, 148
Fischer, D. A., & Valenti, J. 2005, ApJ, 622, 1102
Garwood, F. 1936, Biometrika, 28, 437
Girardi, L., Groenewegen, M. A. T., Hatziminaoglou, E., & da Costa, L. 2005, A&A, 436, 895
Guzik, P., Drahus, M., Rusek, K., et al. 2020, Nat. Astron., 4, 53
Hanse, J., Jílková, L., Portegies Zwart, S. F., & Pelupessy, F. I. 2018, MNRAS, 473, 5432
Hazen, R. M., & Roedder, E. 2001, Nature, 411, 155
Helmi, A. 2020, ARA&A, 58, 205
Hoover, D. J., Seligman, D. Z., & Payne, M. J. 2022, PSJ, 3, 71
Horne, W. H., Volpe, R. P., Korza, G., et al. 2022, Astrobiology, 22, 1337
Horneck, G., Rettberg, P., Reitz, G., et al. 2001, Orig. Life Evol. Biosph., 31, 527
Horneck, G., Stöffler, D., Ott, S., et al. 2008, Astrobiology, 8, 17
Hui, M.-T., Jewitt, D., Mutchler, M. J., Agarwal, J., & Kim, Y. 2026, ApJL, 999, L37
Ivezić, Ž., Kahn, S. M., Tyson, J. A., et al. 2019, ApJ, 873, 111
Kakharov, S., & Loeb, A. 2026, A&A, 709, A178
Klenner, F., Bönigk, J., Napoleoni, M., et al. 2024, Sci. Adv., 10, eadl0849
Kminek, G., Bada, J. L., Pogliano, K., & Ward, J. F. 2003, Radiat. Res., 159, 722
Loeb, A. 2025, RNAAS, 9, 178
Marčeta, D., & Seligman, D. Z. 2023, PSJ, 4, 230
Meech, K. J., Weryk, R., Micheli, M., et al. 2017, Nature, 552, 378
Melosh, H. J. 2003, Astrobiology, 3, 207
Mileikowsky, C., Cucinotta, F. A., Wilson, J. W., et al. 2000, Icarus, 145, 391
Morono, Y., Ito, M., Hoshino, T., et al. 2020, Nat. Commun., 11, 3626
Pavlov, A. K., et al. 2022, Astrobiology, 22, 1099
Petigura, E. A., Marcy, G. W., Winn, J. N., et al. 2018, AJ, 155, 89
Price, P. B., & Sowers, T. 2004, Proc. Natl. Acad. Sci. USA, 101, 4631

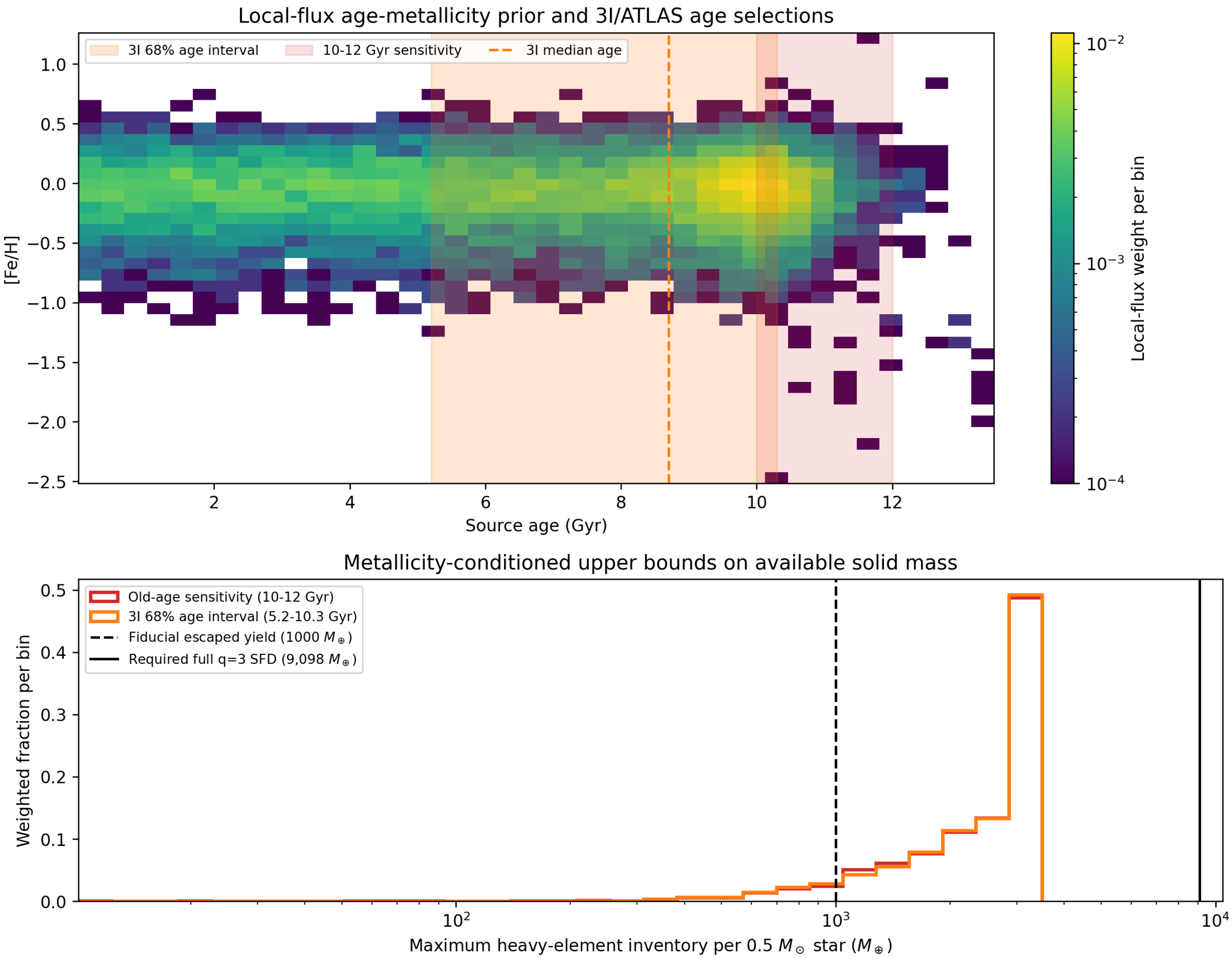

Fig. 7: Top: nominal local-flux age-metallicity prior with the published 3I/ATLAS 68% age interval, its 8.7 Gyr median, and a 10–12 Gyr old-age sensitivity. Bottom: heavy-element inventory ceilings inferred from $Z_{\rm upper} = \min[0.02, 0.02\,10^{[\rm Fe/H]}]$ for an adopted $0.5\,M_\odot$ source star. The distributions assume that every heavy element is available for escaped ISOs; the vertical lines mark the fiducial $1000\,M_\oplus$ yield and the required $9098\,M_\oplus$ full $q = 3$ mass.

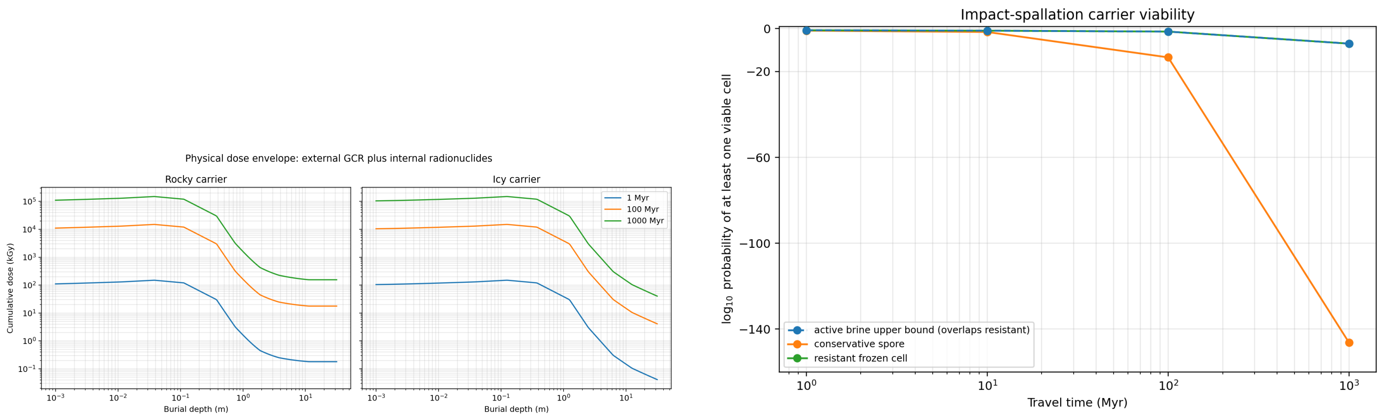

Fig. 8: Left: cumulative physical dose versus burial depth for rocky and icy carriers at 1, 100, and 1000 Myr. The curves combine the external cosmic-ray transport envelope with the internal radionuclide floor. Right: $\log_{10} P$ for the impact-spallation branch at fixed travel times of 1, 10, 100, and 1000 Myr, where P is the probability of retaining at least one viable cell. Conservative spores, resistant frozen cells, and the active-brine upper bound are shown separately. Values include initial population size and launch survival; they are conditional on the route having loaded the object.

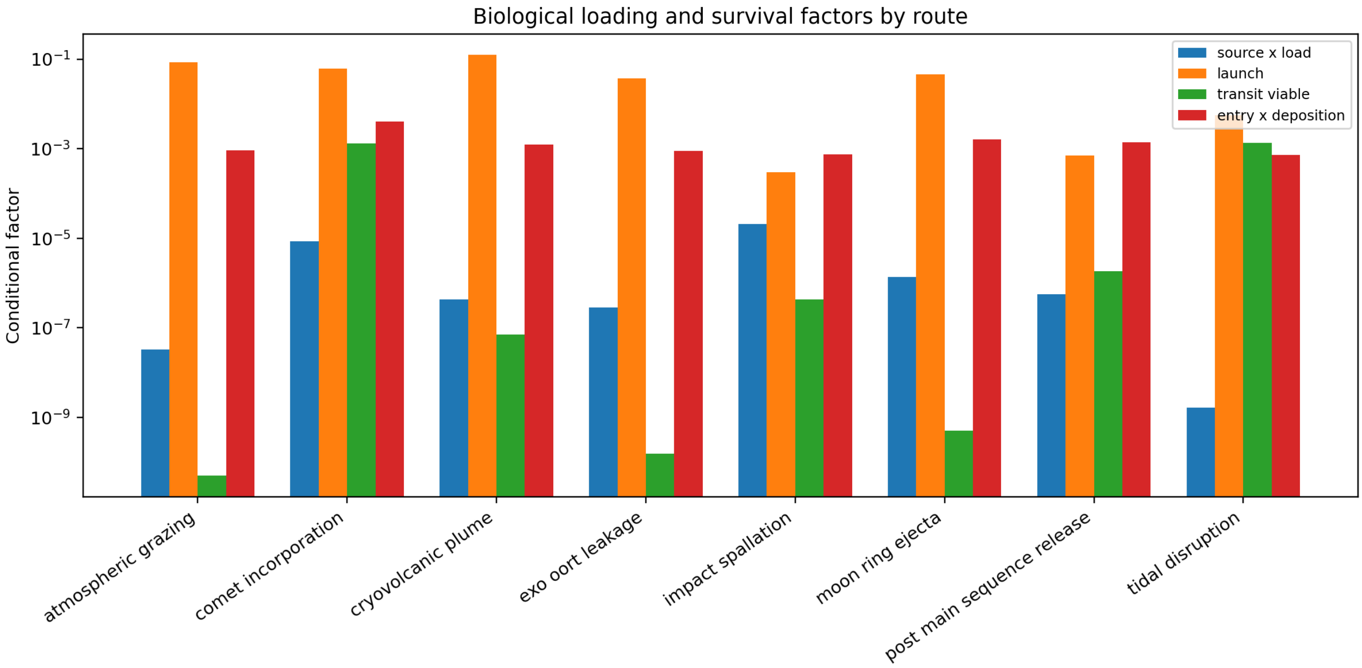

Fig. 9: Source access and loading, launch, transit viability, and entry times deposition for each loading route in the local-flux, late-uniform, conservative-spore sample. Transit viability uses the sampled late-uniform travel times (mean 3.2 Gyr; median 2.7 Gyr), not a fixed 1 Gyr lifetime. These are conditional factors and do not include the unknown fraction of inhabited systems.

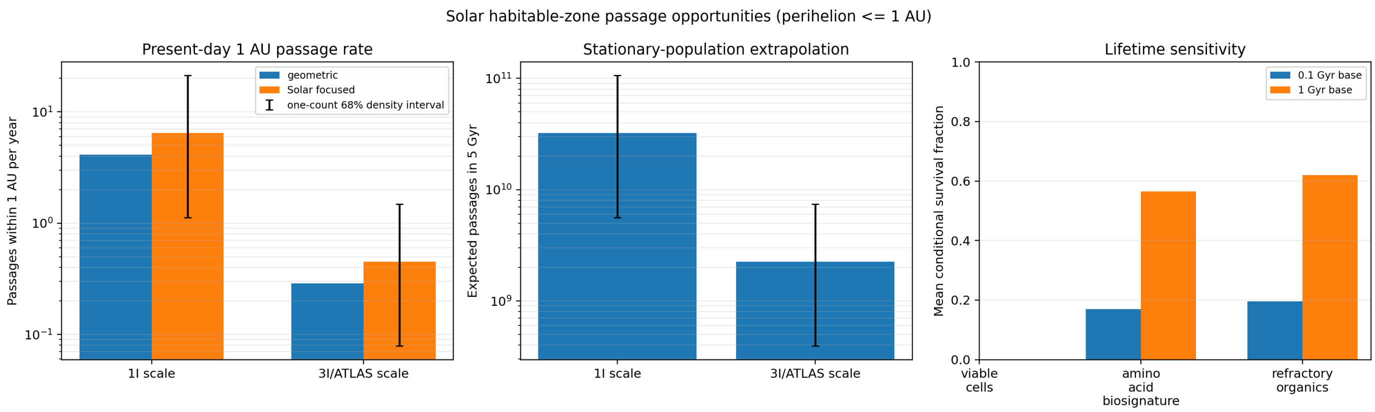

Fig. 10: Solar passages within 1 AU. Left: present-day geometric and gravitationally focused rates for the separate 1I-scale and 3I/ATLAS-scale normalizations; error bars show the external one-count 68% density interval. Middle: focused counts extrapolated over 5 Gyr under a stationary population. Right: conditional survival fractions for 0.1 and 1 Gyr base lifetimes, averaged over the three ejection histories and the two displayed size classes. A 1 AU passage is treated as an optimistic heating and release opportunity, not as interception by a planet.

Raymond, S. N., Armitage, P. J., Veras, D., Quintana, E. V., & Barclay, T. 2018, MNRAS, 476, 3031
Schönrich, R., Binney, J., & Dehnen, W. 2010, MNRAS, 403, 1829
Seligman, D. Z., Micheli, M., Farnocchia, D., et al. 2025, ApJL, 989, L36
Siraj, A., & Loeb, A. 2020, Life, 10, 44
Thoss, V., Loeb, A., & Burkert, A. 2026, arXiv e-prints, arXiv:2603.15735
Veras, D., Evans, N. W., Wyatt, M. C., & Tout, C. A. 2014, MNRAS, 437, 1127
Vreeland, R. H., Rosenzweig, W. D., & Powers, D. W. 2000, Nature, 407, 897
Wallis, M. K., & Wickramasinghe, N. C. 2004, MNRAS, 348, 52
Wang, J., & Fischer, D. A. 2015, AJ, 149, 14
Willett, E., Miglio, A., Mackereth, J. T., et al. 2023, MNRAS, 526, 2141
Zhang, D.-C., Brouchkov, A., Griva, G., Schinner, F., & Margesin, R. 2013, Biology, 2, 85

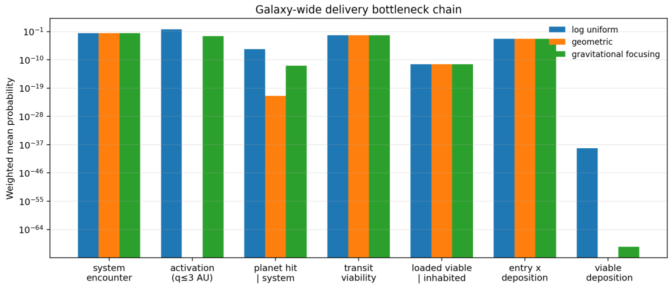

Fig. 11: Weighted factors along the delivery chain for the nominal mission-accessible, late-uniform, resistant frozen-cell impact-spallation branch. Travel times are sampled from the late-uniform ejection history up to the source-star age; they are not fixed at 1 Gyr. For this branch the mean sampled travel time is 3.3 Gyr (median 2.6 Gyr). "Loaded viable" is conditional on an inhabited source, and the final stage includes entry and deposition but not successful establishment. The geometric and focusing endpoints are limited by rare-event sampling as well as by the adopted narrow debris geometry.